

Comparison of characteristics of selected metallic and metal oxide nanoparticles produced by picosecond laser ablation at 532 and 1064 nm wavelengths

Abubaker Hamad¹ · Lin Li¹ · Zhu Liu^{1,2}

Received: 19 May 2016 / Accepted: 7 September 2016 / Published online: 20 September 2016
© The Author(s) 2016. This article is published with open access at Springerlink.com

Abstract Picosecond laser generation of nanoparticles was only recently reported. The effect of laser wavelength in picosecond laser generation of nanoparticles is not yet fully understood. This investigation reports the new findings comparing the characteristics of Au, Ag, Ag–TiO₂, TiO₂, ZnO and iron oxide nanoparticles generated by picosecond laser ablation in deionised water at 532 and 1064 nm laser wavelengths. The laser ablation was carried out at a fixed pulse width of 10 ps, a repetition rate of 400 kHz and a scan speed of 250 mm/s. The nanoparticles were characterised by UV–Vis optical spectroscopy, transmission electron microscopy (TEM) and X-ray diffraction (XRD). The work shows that there is no noticeable difference in the size of the metal oxide nanoparticles produced at 532 and 1064 nm, especially for the TiO₂ and ZnO nanoparticles; however, a considerable size difference can be seen for metallic (e.g. Au) and metallic compound (e.g. Ag–TiO₂) nanoparticles at the two wavelengths. It demonstrates that noble metals are more profoundly affected by laser wavelengths. The reasons behind these results are discussed. In addition, the work shows that there are different crystalline structures of the TiO₂ nanoparticles at 1064 and 532 nm wavelengths.

1 Introduction

Laser ablation in deionised water has been used widely to produce metallic, bi-metallic and tri-metallic nanoparticles as well as metal oxides [1]. An advantage of laser production of nanoparticles is the high purity of the nanoparticles produced, special surface charge characteristics and easy preparation in comparison with chemical methods. It was found that various laser parameters such as laser power, energy density (fluence), beam spot size, scanning speed and media under which ablation takes place and wavelength [2, 3], may be used to manipulate the size distribution and shape of the nanoparticles.

Nanosecond and picosecond lasers with different wavelengths have been used to produce different types of nanoparticles, although very few studies used picosecond lasers. For example, Baladi and Mamoori [4] used a nanosecond laser to produce Al nanoparticles at 1064 and 533 nm wavelengths in ethanol. It was shown that finer spherical particles and a higher rate of production of the nanoparticles can be produced at 1064 than at 533 nm. In addition, it was shown that higher productivity and larger nanoparticles were produced at higher laser energy. Mortazavi et al. [5] produced smaller-sized palladium (Pd) nanoparticles at a greater production rate with a nanosecond laser in deionised water at 1064 nm (IR-Nd:YAG laser) than at 193 nm (UV ArF Excimer laser). It was also shown that the plasma temperature of the longer wavelength was considerably higher than that of the shorter wavelength because of the higher inverse Bremsstrahlung reaction rate to heat the induced plasma. In addition, the blue shift phenomena that occurred at the longer laser wavelength is evident that the plasma produced at 1064 nm is more energetic than that produced at 193 nm. Furthermore, Kim et al. [6] studied the effects of using a

✉ Abubaker Hamad
abubaker.hamad75@yahoo.co.uk

¹ Laser Processing Research Centre, School of Mechanical, Aerospace and Civil Engineering, The University of Manchester, Manchester M13 9PL, UK

² School of Materials, The University of Manchester, Manchester M13 9PL, UK

nanosecond laser of different laser wavelengths and laser fluence on the production of palladium (Pd) nanoparticles in distilled water. It was found that the Pd nanoparticles produced at 532 and 355 nm wavelengths are more homogenous and smaller in size than those produced at 1064 nm. It was concluded that increasing laser fluence leads to an increase in the size of the nanoparticles at all wavelengths. Chewchinda et al. [7] prepared the characteristics of spherical Si nanoparticles with nanosecond laser ablation in ethanol (10 ns and 10 Hz) at 532 and 1064 nm laser wavelengths under the same energy density (1.2 J/cm^2). It was found that smaller nanoparticles and a narrower size distribution of Si nanoparticles were produced at 532 nm than those at 1064 nm; the average sizes were about 3 and 7 nm, respectively. In addition, a higher concentration of nanoparticles was obtained at shorter laser wavelengths. Imam et al. [2] found that smaller Au nanoparticles and a higher rate of productivity were generated by nanosecond laser ablation in water at 532 nm than those produced at 1064 nm wavelength. He et al. [8] produced ZnO nanoparticles by nanosecond laser ablation in a liquid medium at a wavelength of 355 nm.

Intartaglia et al. [9] produced Au–Ag nanoparticles by picosecond laser ablation in a liquid environment from an Ag target placed in a colloidal Au nanoparticles irradiated at different laser wavelengths. It was shown that the average size of the nanoparticles did not depend on the laser wavelength; their average sizes were 5, 15 and 8.5 nm at 355, 532 and 1064 nm laser wavelengths, respectively. The picosecond laser operated at a laser pulse width of 60 ps and a repetition rate of 20 Hz with maximum pulse energy of 115 mJ at 1064 nm, 55 mJ at 532 nm and 35 mJ at 355 nm wavelengths. Giorgetti et al. [10] prepared nanoparticles by picosecond laser ablation of metallic (Au and Ag) and semiconductor (CdSe) target materials in water at fundamental (1064 nm–25 ps), second-harmonic (532 nm–20 ps) and third-harmonic (355 nm–15 ps) laser wavelengths. Different sizes of Au nanoparticles were produced: 5.2, 3.2 and 2.5 nm at 1064, 532 and 355 nm wavelengths, respectively. Hamad et al. [11] produced Ag–TiO₂ compound nanoparticles by picosecond laser ablation of an Ag/Ti alloy target in deionised water at a wavelength of 1064 nm [11]. Silver nanoparticles have been produced by a picosecond laser in a liquid environment at wavelengths of 1064 nm [12], 1030 and 515 nm [13]. Giorgetti et al. [10] produced Ag nanoparticles at 1064 nm and post-irradiated them at a wavelength of 532 nm, and Nouneh et al. [14] used the 532-nm wavelength of a picosecond laser to post-irradiate the Ag nanoparticles on an indium tin oxide (ITO) substrate in an attempt to manipulate their size and change their optical absorption properties. Schwenke et al. [13] produced Ag nanoparticles in polyurethane-doped tetrahydrofuran at 1030 and 515 nm wavelengths of

a picosecond laser (7 ps), and Menéndez-Manjón et al. [15] produced Au, Ag and AuAg alloy nanoparticles using a picosecond-pulsed laser (7 ps) at a wavelength of 515 nm in liquid monomer. Liu et al. [16] produced FeO nanoparticles by a picosecond laser in poly(vinylpyrrolidone) (PVP) solution at a wavelength of 1064 nm. They showed that the stability and particle size of the colloidal nanoparticles can be controlled via the PVP concentration because of the repulsive interaction and capping effects of PVP solution.

Despite the previous studies on laser wavelength effects in laser production of nanoparticles, the effect of laser wavelength in picosecond laser production of nanoparticles is not yet clear and the mechanisms involved are not clear. In this work, picosecond laser wavelengths of 532 and 1064 nm were used to produce Au, Ag, Ag–TiO₂, TiO₂, ZnO and iron oxide nanoparticles in deionised water. The nanoparticles were then compared in terms of their sizes and morphology.

2 Experimental materials and procedure

2.1 Materials

An Au target foil with dimensions of 65 mm × 10 mm × 0.2 mm with a purity of 99.99 %, an Ag target plate with dimensions of 25 mm × 25 mm × 2 mm and a purity of 99.99 %, a Ti/Ag alloy plate (3:1 at.%) with the dimensions of 25 mm × 25 mm × 1 mm and Ag and Ti alloy components with purity levels of 99.95 and 99.7 %, respectively, a Ti target plate with the dimensions of 25 mm × 25 mm × 1 mm and a purity of 99.99+ %, a Fe target foil with the dimensions of 30 mm × 30 mm × 0.3 mm with a purity of 99.95 %, and a Zn target plate with the dimensions of 25 mm × 25 mm × 2 mm with a purity of 99.99+ % were used to generate the Au, Ag, Ag–TiO₂, TiO₂, ZnO and iron oxide nanoparticles in deionised water.

2.2 Nanoparticle Production Procedure

In this work, Au, Ag, Ag–TiO₂, TiO₂, ZnO and iron oxide nanoparticles were produced via a dual-wavelength picosecond laser with wavelengths of 532 and 1064 nm (see Fig. 1a), respectively, in distilled water. The liquid solution was in the stationary condition. The target materials were placed individually on a stainless steel holder in a 100-ml Pyrex glass vessel which contained 15–20 ml of distilled water. The water level above the targets was fixed at around 2 mm in all experiments. The experimental set-up is shown in Fig. 1b. The ablation area was 5 mm × 5 mm with a galvo scanning computer program, but on the surface of the samples it was approximately 3 mm × 3 mm at the

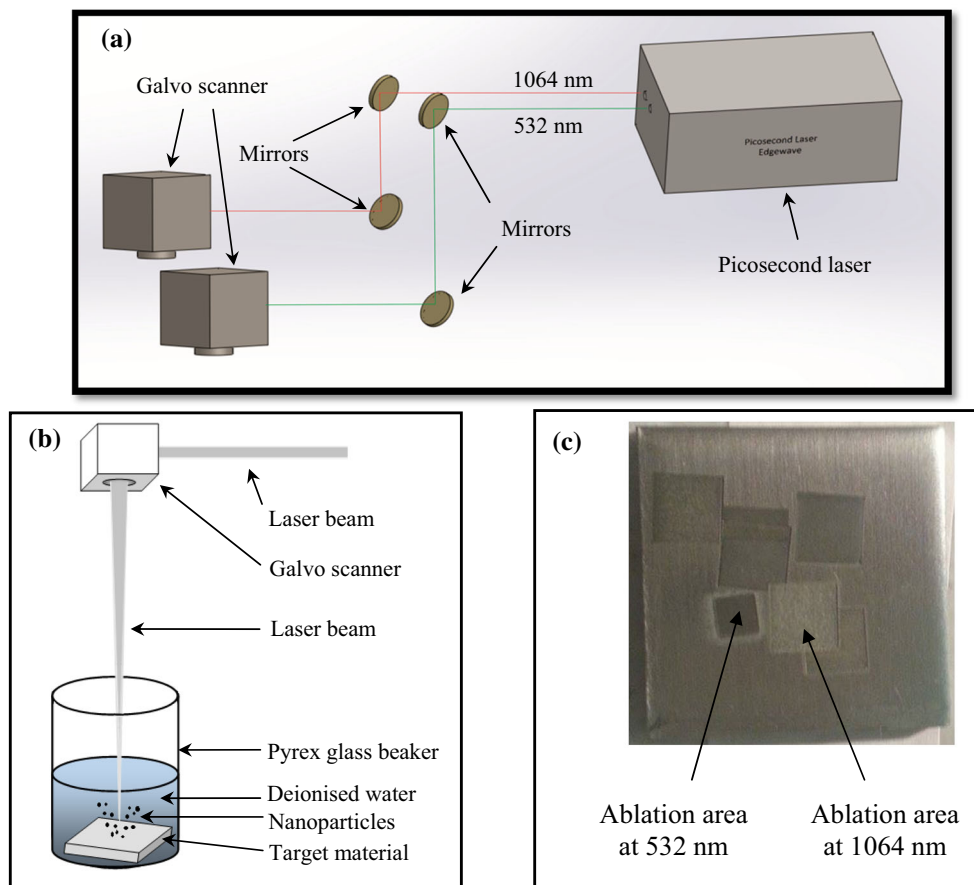


Fig. 1 Scheme of the picosecond laser with dual wavelength (a), experimental set-up for nanoparticle production (b) and ablation area on a sample at 532 and 1064 nm wavelengths (c)

wavelength of 532 nm and $4.65 \text{ mm} \times 4.65 \text{ mm}$ at 1064 nm (see Fig. 2c). Further details of the laser beam characteristics at both wavelengths are summarised in Table 1. Galvo scanners (SCANLAB hurry SCAN 20) were used to scan the laser beams over the target area in a raster pattern at both wavelengths.

2.3 Material Characterisation and Sample Preparation Procedure

The nanoparticles produced were characterised with a UV–Vis spectrometer (Analytic Jena, SPECORD 250, dual beam) in order to measure the absorption spectra of the colloidal nanoparticles. A transmission electron microscope (TEM) [Philips CM20 200 kV TEM (LaB6)] was used to examine the morphology and size distribution of the nanoparticles. X-ray diffraction (XRD) (BrukerD8-Discover, step size $[\text{2}\theta] = 0.0200$) was used to investigate the crystalline structures of the nanoparticles. A copper micro-grid mesh (200 mesh) was used to prepare samples for the TEM analysis. The mesh was put on a glass slide on a hot plate. After depositing a drop of colloidal nanoparticles onto the mesh, the hot plate was turned on and the

temperature was raised to about $45 \text{ }^\circ\text{C}$. Before drying the drop completely, the mesh was wiped across the drop to collect more nanoparticles and disperse the nanoparticles uniformly, and then the drop was allowed to dry completely. This process was repeated twice to deposit a sufficient amount of nanoparticles on the copper microgrid mesh. The X-ray diffraction samples were prepared on glass slides; first, the colloidal nanoparticles were centrifuged for about 15 min using a microcentrifuge machine; then, they were dropped onto a glass slide and allowed to dry on a hot plate at about $40 \text{ }^\circ\text{C}$. This process was repeated several times to deposit a sufficient amount of nanoparticles on the slide.

3 Results

3.1 Au Nanoparticles

Figure 2a shows the optical absorption spectra of Au nanoparticles produced at 532 and 1064 nm in deionised water. The surface plasmon resonance of the nanoparticles was observed at 520 and 530 nm at the laser wavelengths

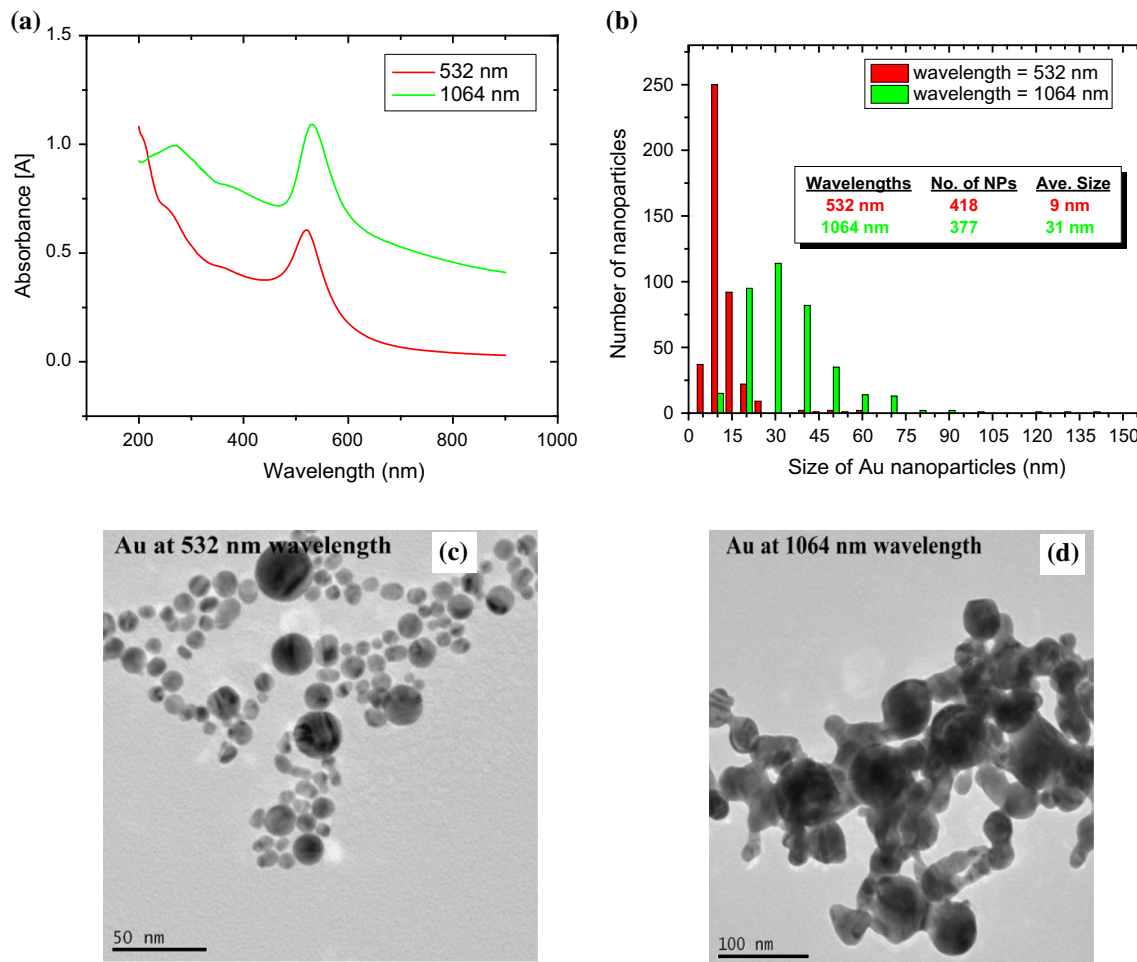


Fig. 2 Optical absorption spectra (a), histogram of the size distribution (b) and TEM images (c, d) of the Au nanoparticles produced by a picosecond laser at 532 and 1064 nm wavelengths in deionised water

Table 1 Characteristics and process parameters of the picosecond laser at both wavelengths (532 and 1064 nm)

Laser parameters	Wavelengths	
	532 nm	1064 nm
Average power (P)	16.7 W	27.5 W
Frequency (f)	400 kHz	400 kHz
Laser pulse duration (τ)	10 ps	10 ps
Beam diameter at the laser output window	3 mm	3 mm
Focal length	100 mm	163 mm
Spot size (D)	32.5 μm	106 μm
Scan speed (v)	250 mm/s	250 mm/s
Laser pulse energy (E_{pulse})	42 μJ	69 μJ
Laser fluence (F_{laser})	5 J/cm^2	0.8 J/cm^2

of 532 and 1064 nm, respectively. For the Au nanoparticles produced at the 532-nm laser wavelength, the intensity of optical absorption spectrum of the Au nanoparticles was reduced sharply, while at 1064 nm it increased and then

decreased slowly. Figure 2b shows the histogram of the size distribution. It can be noted that the Au nanoparticles produced at 532 nm are smaller in size than those produced at 1064 nm, measuring 9 and 31 nm, respectively, despite the fact that the laser fluence at 532 nm was much higher than that at 1064 nm showing more dominating effect of laser wavelength. Only about 4 % of the Au NPs (generated at 532 nm) are larger than 20 nm. As shown in Fig. 2c, d, the Au nanoparticles generated at the shorter wavelength are more uniformly dispersed than those generated at the longer wavelength. The longer wavelength produced a chain of nanoparticles, with most of them agglomerated together. Meanwhile, the nanoparticles produced at the shorter wavelength can be seen individually.

3.2 Ag–TiO₂ Compound Nanoparticles

As shown in Fig. 3a, in general, the optical absorption spectra of Ag–TiO₂ compound nanoparticles produced by picosecond laser ablation in deionised water at 532 and

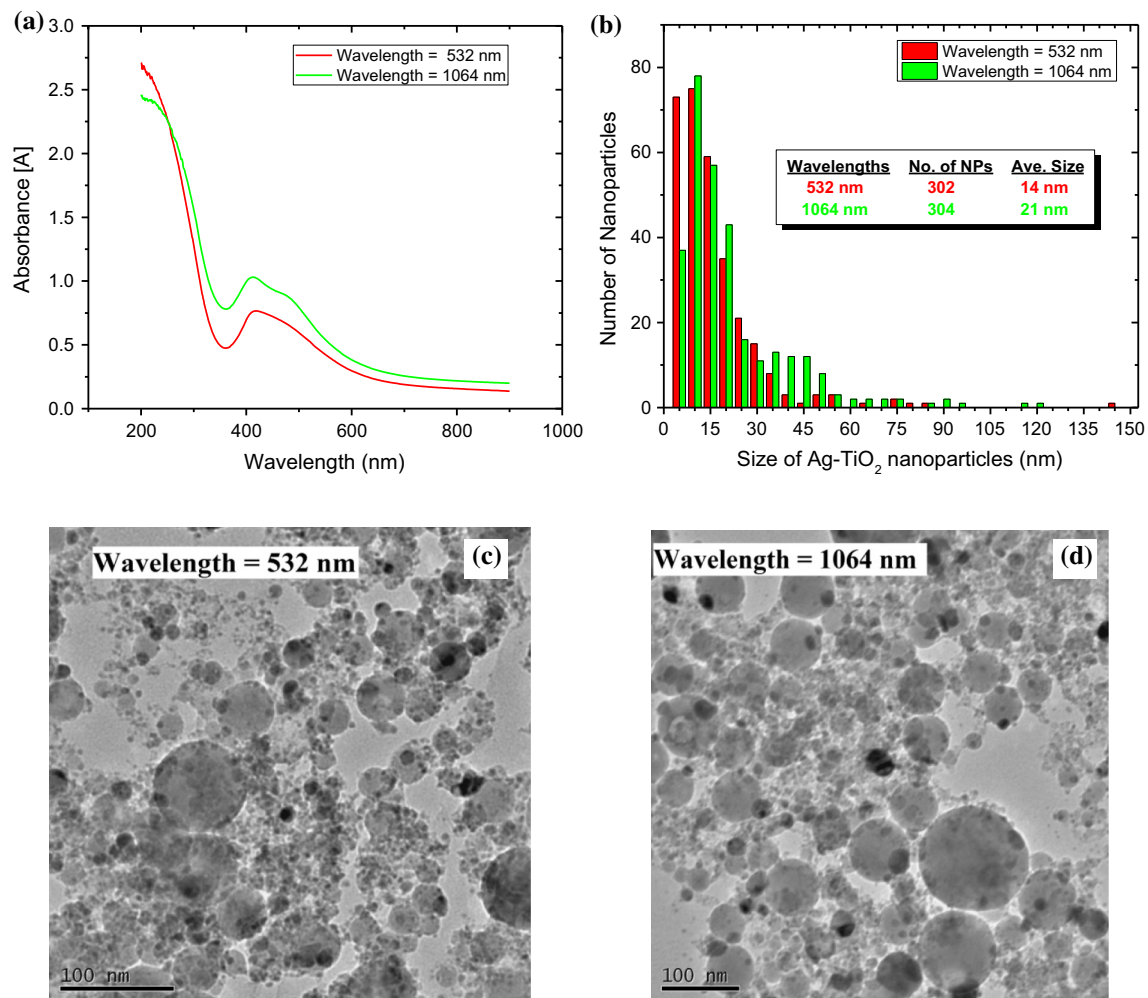


Fig. 3 Optical absorption spectra (a), histogram of the size distribution (b) and TEM images (c, d) of the Ag-TiO₂ nanoparticles produced by a picosecond laser at 532 and 1064 nm wavelengths in deionised water

1064 nm were similar, but the nanoparticles produced at the shorter wavelength had a slightly sharper plasmon peak (at 400 nm) than that produced at the longer wavelength. The surface plasmon resonance of the nanoparticles at 532 and 1064 nm started at 410 and 415 nm, respectively, extending to about 500 nm in the visible range.

The histogram of the size distribution in Fig. 3b shows that the 532-nm wavelength produced nanoparticles with a smaller average size (14 nm) in comparison with those produced at 1064 nm (21 nm). As shown in the TEM images (Fig. 3c, d), spherical Ag-TiO₂ nanoparticles were produced at both wavelengths.

3.3 TiO₂ Nanoparticles

Figure 4a shows the optical absorption spectra of TiO₂ nanoparticles produced at 532 and 1064 nm in deionised water. The difference between the optical absorption spectra of the colloidal TiO₂ nanoparticles generated at

both wavelengths can be seen in the UV range. For nanoparticles produced at the 532-nm wavelength, the spectrum intensity dropped sharply at the UV wavelength earlier than those produced at 1064 nm wavelength. Both spectra have the same characteristics in the visible range. In spite of their different optical absorption spectra, the histogram of the size distribution (Fig. 4b) shows that there is a similarity between the size distributions of the TiO₂ nanoparticles generated at both laser wavelengths, in that the average size and size distribution are close to each other. The average sizes of the nanoparticles produced at the 532 and 1064 nm were 34 and 32 nm, respectively. The TEM images (Fig. 4c, d) show that spherical TiO₂ nanoparticles were produced at both wavelengths.

Figure 5 shows the XRD pattern of the TiO₂ nanoparticles produced at different wavelengths. The nanoparticles produced at 532 nm wavelength are crystalline with mixed anatase, rutile and brookite phases, but the nanoparticles produced at 1064 nm wavelength are crystalline with

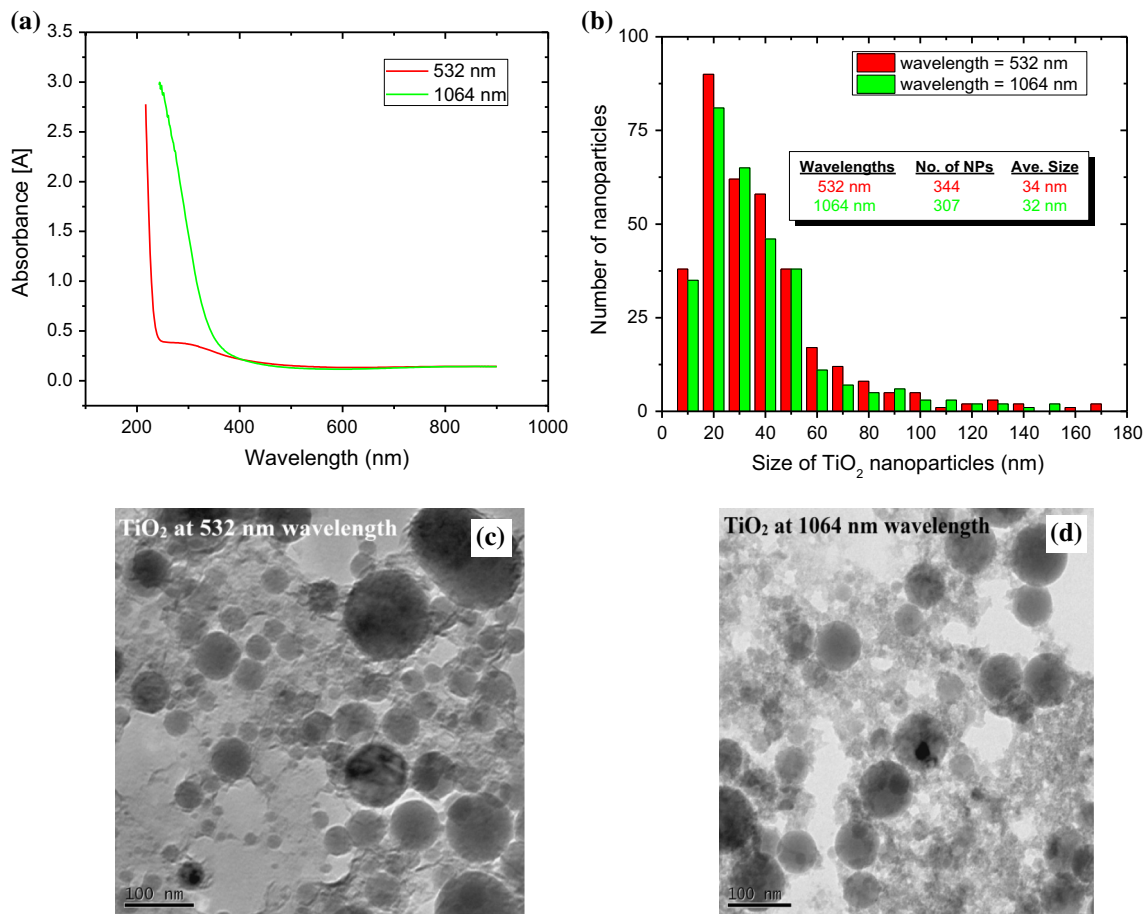


Fig. 4 Optical absorption spectra (a), histogram of the size distribution (b) and TEM images (c, d) of the TiO₂ nanoparticles produced by a picosecond laser at 532 and 1064 nm wavelengths in deionised water

mixed rutile and brookite. In general, the same peaks were not observed in both samples; thus, the samples have not the same crystalline phases. In other words, the change in laser wavelengths has a noticeable effect on the phase of the TiO₂ nanoparticles.

The peak positions $2\theta = 37.5^\circ$ and 63.3° are attributed to the anatase TiO₂ phases (004) and (204), respectively [17, 18]. The peak positions $2\theta = 36^\circ$, 41° , 54° and 63.85° are attributed to the rutile TiO₂ phases (101), (111), (211) and (310), respectively [17, 19]. In addition, the peaks at $2\theta = 32.5^\circ$ are indicative of the brookite phase of the TiO₂ nanoparticles [20, 21]. A strong rutile peak was observed for the 532-nm laser wavelength at 27.5° [22]. In addition, small peaks at 48° and 68.3° were observed at 532 nm which indicate the anatase phase [23, 24], and the peaks at 56.25° and 70° represent the rutile phase [23, 25] of the TiO₂ nanoparticles.

3.4 Iron Oxide Nanoparticles

Figure 6a shows the optical absorption spectra of iron oxide nanoparticles produced at 532 and 1064 nm in

deionised water. Both sets of nanoparticles have almost exactly the same characteristics. The histogram of the size distribution (see Fig. 6b) shows that smaller iron oxide nanoparticles were produced at 1064 nm, measuring about 21 nm in average size in comparison with those produced at 532 nm (about 28 nm in average size). It can be observed that more than 50 % of the measured nanoparticles measured under 20 nm. The TEM images (Fig. 6c, d) show that spherical iron oxide nanoparticles were produced at both wavelengths. The nanoparticles are magnetic.

Figure 7 shows the X-ray diffraction of the iron oxide nanoparticles produced by picosecond laser in deionised water with different wavelengths (532 and 1064 nm). The nanoparticles are crystalline with mixed Fe, FeO and Fe₃O₄. The peak positions of $2\theta = 18.28^\circ$, 30° , 35.42° , 43° , 53.4° , 56.92° , 62.5° and 73.95° are attributed to the anatase Fe₃O₄ phases (111), (220), (311), (400), (422), (511), (440) and (533), respectively [26, 27]. The peak positions $2\theta = 61^\circ$ (at the 532-nm wavelength) and 73.1° are attributed to the FeO phases (220), and (311), respectively [28, 29]. In addition, the peaks at $2\theta = 44.67^\circ$, 65° and 82.33° are indicative of the Fe phases (110), (200) and

Fig. 5 XRD images of TiO₂ nanoparticles produced by picosecond laser in deionised water with different wavelengths (532 and 1064 nm)

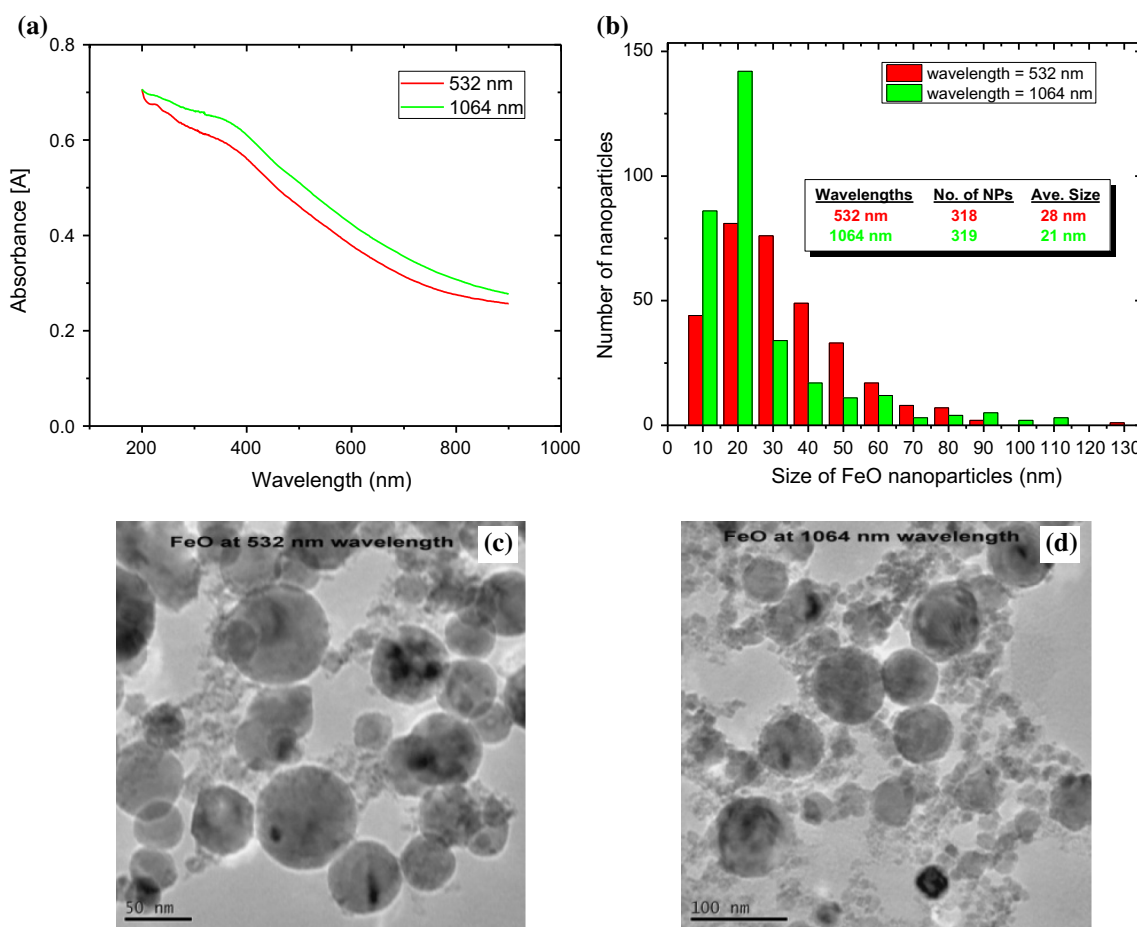
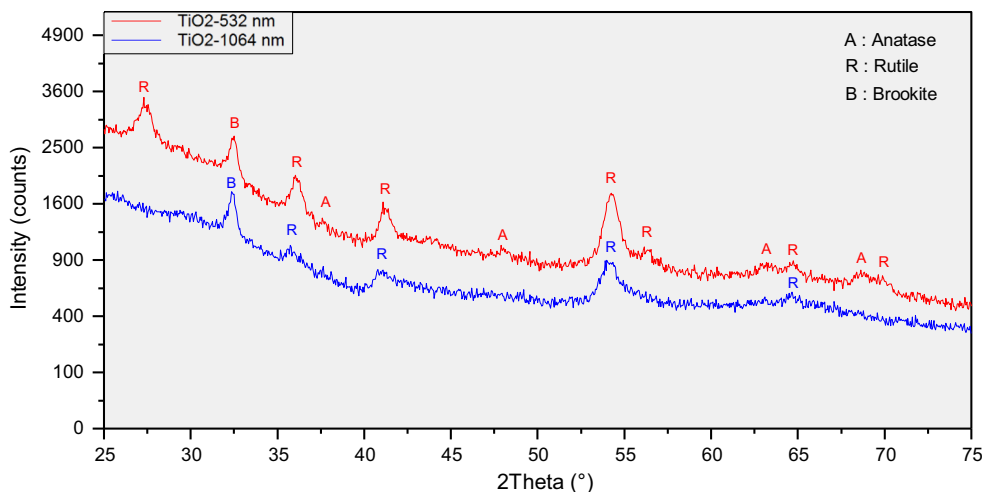


Fig. 6 Optical absorption spectra (a), histogram of the size distribution (b) and TEM images (c, d) of the iron oxide nanoparticles produced by a picosecond laser at 532 and 1064 nm wavelengths in deionised water

(211), respectively [30]. The diffraction peaks at planes (111), (220), (311), (400), (422), (511) and (440) are the characteristic peaks of Fe₃O₄ crystals with a cubic spinel structure and corresponded to a cubic unit cell [26, 31], or the inverse-spinel structure (Fe₃O₄) [32].

3.5 ZnO Nanoparticles

ZnO nanoparticles were produced by the picosecond laser at the two wavelengths noted above. It can be seen from Fig. 8a that their optical absorption spectra are similar,

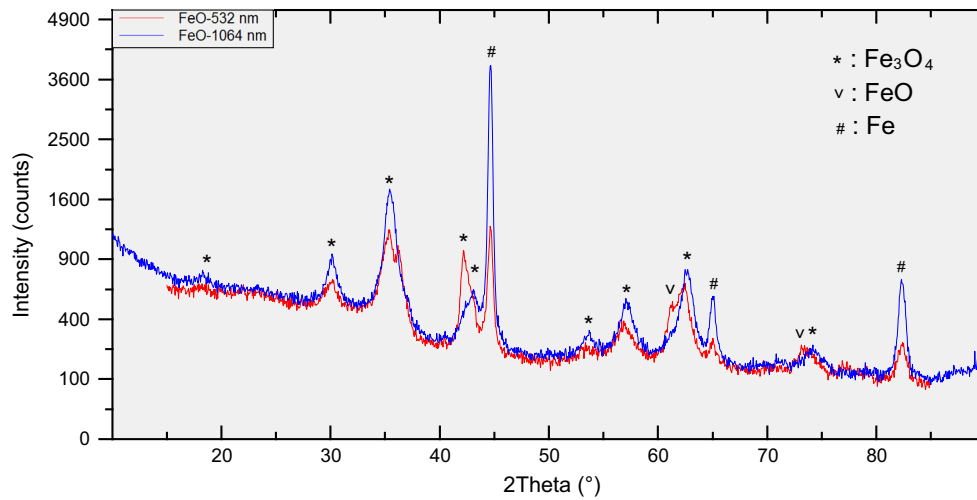


Fig. 7 XRD images of iron oxide nanoparticles produced by picosecond laser in deionised water with different wavelengths (532 and 1064 nm)

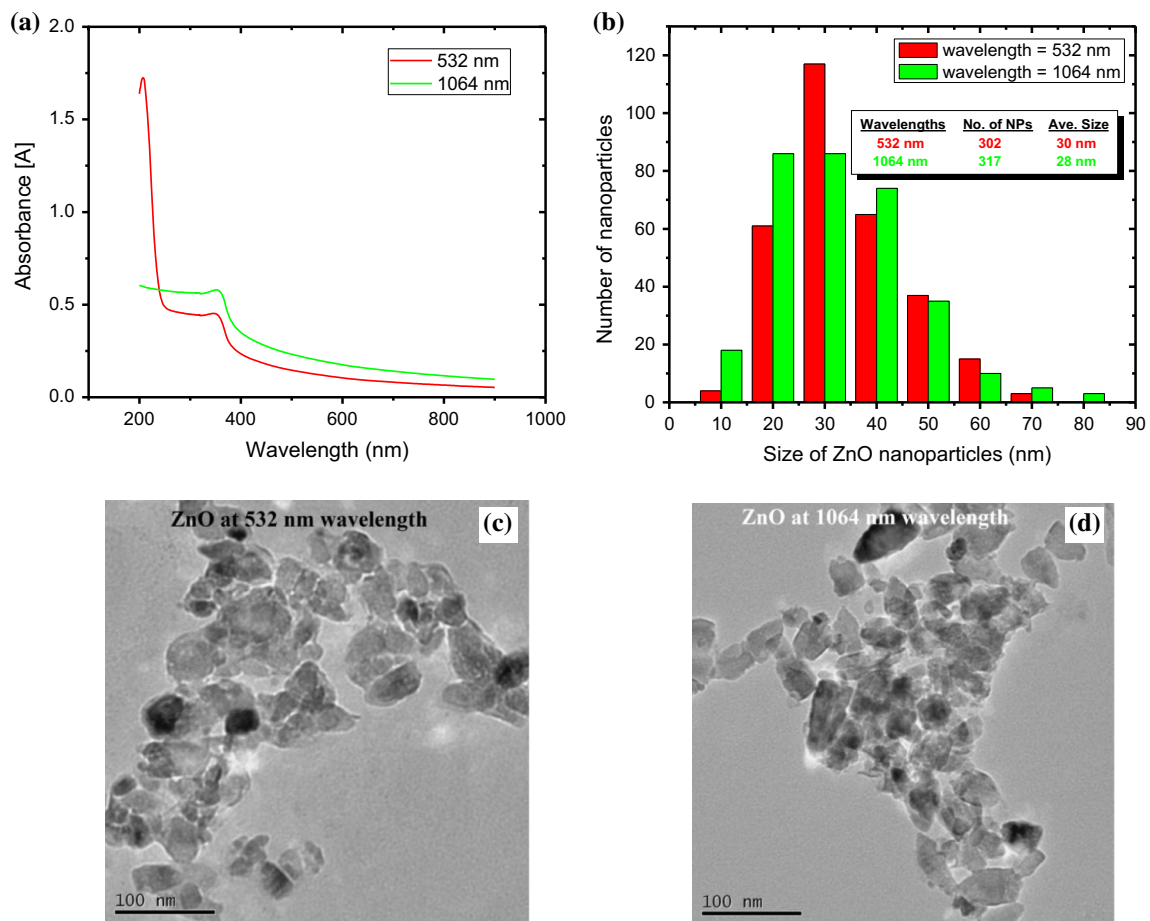


Fig. 8 Optical absorption spectra (a), histogram of the size distribution (b) and TEM images (c, d) of the ZnO nanoparticles produced by a picosecond laser at 532 and 1064 nm wavelengths in deionised water

except in the range of 200–250 nm. The nanoparticles produced at 532 nm initially exhibited higher absorbance, which then decreased sharply. On the other hand, the

intensity of absorption spectrum produced at 1064 nm was initially lower. The histogram of the size distribution in Fig. 8b shows that there is no significant effect of the

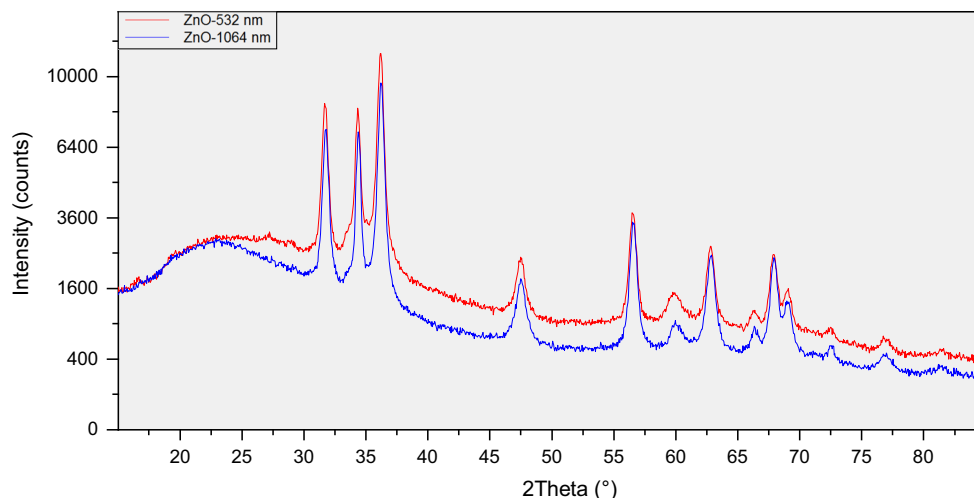


Fig. 9 XRD images of ZnO nanoparticles produced by picosecond laser in deionised water with different wavelengths (532 and 1064 nm)

wavelengths on the size of the nanoparticles. The TEM images (Fig. 8c, d) show that the ZnO nanoparticles have irregular shapes, but the majority are pin-shaped.

Figure 9 shows the XRD of the ZnO nanoparticles produced by picosecond laser in deionised water with different wavelengths (532 and 1064 nm). A number of Bragg reflections with 2θ values of 31.76° , 34.4° , 36.25° , 47.55° , 56.59° , 62.85° , 66.37° , 67.94° , 69° , 72.56° , 76.95° and 81.37° are observed corresponding to (100), (002), (101), (102), (110), (103), (200), (112), (201), (004), (202) and (104) planes, respectively, they showing a typical XRD pattern of ZnO nanoparticles (ICPDS card No. 89.1397) [33]. Almost all the peaks fully match the ZnO hexagonal phase of JCPDF No. 36-1451 [34]. Very similar values have also been reported by Arefi and Saeed [35], Dutta and Bichitra [36] and Prabhu et al. [34]. A peak at 60° was observed at both wavelengths; this might be due to the glass substrate. Here, both spectra had exactly the same characteristics, which indicates that the changing wavelengths have no effect on the crystalline structures of the ZnO nanoparticles.

3.6 Ag nanoparticles

An unexpected finding of this work is the inability to produce silver nanoparticles from a pure silver plate material at the 532-nm wavelength. As shown in Fig. 10a, when attempting the above experiment, the optical absorption spectra of the Ag nanoparticles did not show any peak. This indicates that no silver nanoparticles were present in the solution. Even when the ablation process was continued for about 30 min and carried out at different repetition rates, Ag nanoparticles were not produced and the colour of the solution (deionised water) did not change. In contrast, the optical absorption spectra of the Ag

nanoparticles produced at 1064 nm wavelength showed a strong surface plasmon resonance peak at a wavelength of 405 nm and the colour of the colloidal nanoparticles was yellow. The average size of the Ag nanoparticles produced at the 1064-nm wavelength was 29 nm (see Fig. 10b). As shown in Fig. 10c, the TEM images of the Ag nanoparticles produced at 1064 nm are semispherical in shape, but some have pentagonal and hexagonal shapes.

4 Discussion

4.1 Effects of Wavelengths on the Size of the Nanoparticles

Au, Ag, Ag-TiO₂, TiO₂, ZnO and iron oxide nanoparticles were produced at both laser wavelengths 532 and 1064 nm, with the exception of Ag nanoparticles that could not be produced at the wavelength of 532 nm. The TEM images and the size distribution histogram show that significantly smaller Au and Ag-TiO₂ nanoparticles were produced at 532 nm, although slightly smaller TiO₂, ZnO and iron oxide nanoparticles were produced at 1064 nm. As shown in Table 2, there is no noticeable difference in the size of the metal oxide nanoparticles produced at 532 and 1064 nm, especially for the TiO₂ and ZnO nanoparticles; however, a considerable size difference can be seen for the Au and Ag-TiO₂ nanoparticles. It can therefore be ascertained that noble metals are more profoundly affected by laser wavelengths, as almost all of the small Ag-TiO₂ nanoparticles are Ag [37].

According to the photon energy equation $E = hc/\lambda$, the shorter the photon's wavelengths, the higher its energy. At a wavelength of 532 nm, green laser pulses have higher photon energy (2.33 eV) that reaches the target material in

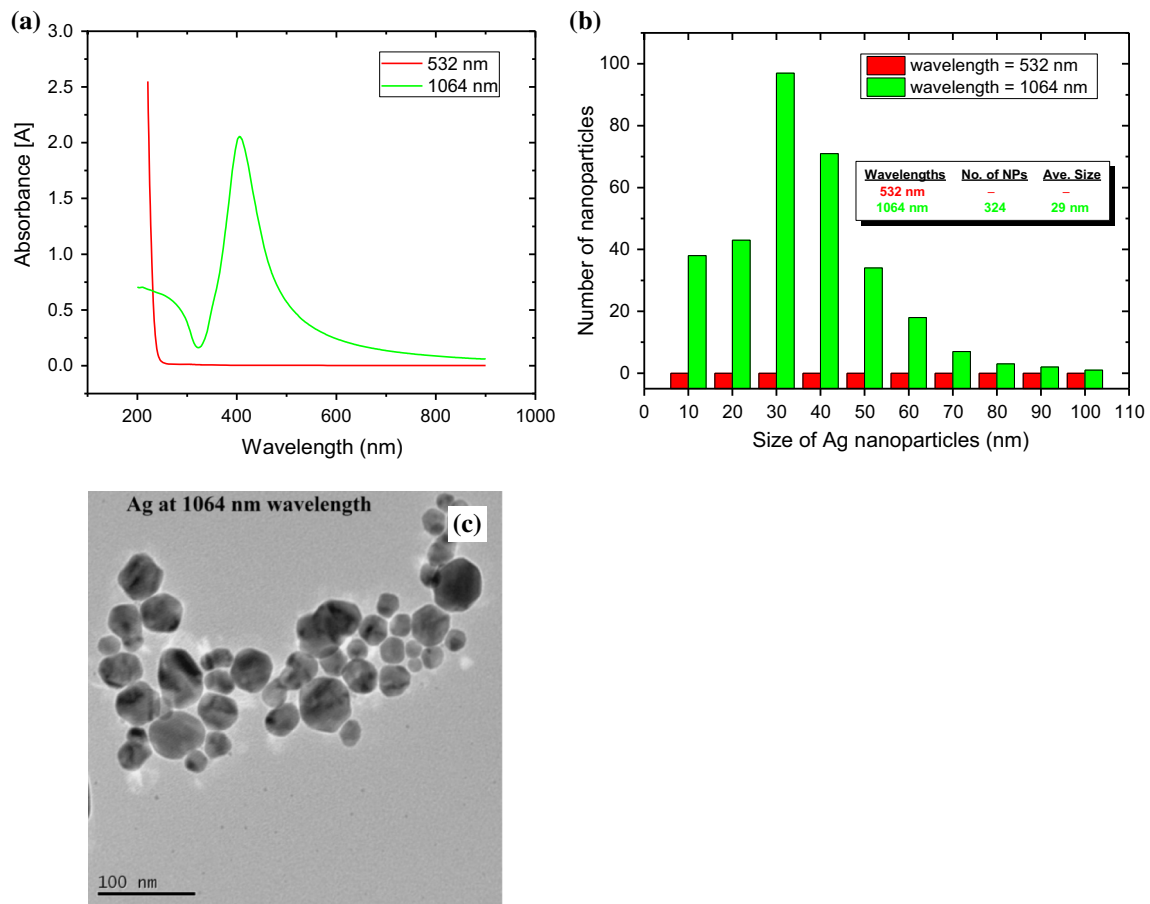


Fig. 10 Optical absorption spectra (a), histogram of the size distribution (b) and TEM images (c) of the Ag nanoparticles produced by a picosecond laser at 1064 nm wavelength in deionised water

Table 2 Average size of Au, Ag–TiO₂, Ag, TiO₂, iron oxide and ZnO nanoparticles produced by picosecond laser at 532 nm and 1064 nm

Nanoparticles	Average size at:		As wavelength increased, the NP size is decreased or increased by	
	532 nm	1064 nm	Decreased	Increased
Au	9 nm	31 nm	–	22 nm
Ag–TiO ₂	14 nm	21 nm	–	7 nm
Ag	–	29 nm	–	–
TiO ₂	34 nm	32 nm	2 nm	–
Iron oxide	28 nm	21 nm	7 nm	–
ZnO	30 nm	28 nm	2 nm	–

comparison with the 1064-nm wavelength, while the IR laser pulses of which have lower photon energy (1.16 eV) reaching the target material. In general, the 532-nm wavelength is more effective at producing smaller Au and Ag nanoparticles than the 1064-nm wavelength. This is because the fragmentation by 1064 nm photons only affects the larger nanoparticles, which have a high extinction coefficient in the near-infrared region. In contrast, the fragmentation produced at 532 nm leads to a reduction in the size of the nanoparticles in the colloidal solution because this wavelength (532 nm) is in the range

of the surface plasmon peak position of the Au and Ag nanoparticles [3]. Au nanoparticles are particularly affected by the 532-nm wavelength, because its surface plasmon resonance is in the range of 532–530 nm, very close to the 532-nm wavelength. It is worth mentioning that the Ag nanoparticles were produced with a Ti/Ag alloy material target, but no Ag nanoparticles were produced with pure Ag target material in deionised water at 532 nm wavelength. Even when the laser parameters such as power and frequency were changed, the Ag nanoparticles were not generated when using pure Ag target plate. The reason

behind this is the changing physical properties of the Ag in Ti/Ag alloy material, because the grindability of some Ti/Ag alloy materials is superior to pure titanium, which leads to a “decrease in the elongation caused by the precipitation of small amounts of fine intermetallic compounds” [38]. The grindability may act as a driving force on the Ag material, causing it to be released from the target material, or the ablation of both Ag and Ti as an intermetallic compound such as AgTi₃, as it is a composition of the Ti/Ag alloy sample target [11]. Here the Ag–TiO₂ nanoparticles are also smaller because they have strong wide peak spectra, extending from 400 to 500 nm (see Fig. 3a).

Ag nanoparticles were not produced at the 532-nm wavelength with the picosecond laser (10 ps). This may be a result of the strong absorption of silver due to their surface plasmon resonance, as Schwenke et al. [13] showed that the productivity of silver nanoparticles at a 515-nm wavelength of a picosecond laser decreases over the ablation process time, while at 1030 nm the productivity is constant. Another reason behind the failure to produce Ag nanoparticles at the 532-nm wavelength might be due to the saturable and reverse saturable absorption in silver nanoparticles at 532 nm using picosecond laser pulses; this phenomenon was observed by Gurudas et al. [39] in Ag nanodots prepared using the pulsed laser deposition method.

Au nanoparticles are more affected by the wavelengths than the other types. A red shift can be seen in the optical absorption spectra of the Au nanoparticles as the nanoparticle production laser wavelength is increased from 532 to 1064 nm. This means that smaller Au nanoparticles are produced at the shorter wavelength. In addition, the shorter wavelength produced a narrower size distribution with separate nanoparticles in comparison with those produced at the longer wavelength which formed particle chains. In addition to the proximity of the 532-nm wavelength to the surface plasmon resonance peak of Au nanoparticles, another reason behind the smaller size of these nanoparticles at this wavelength might be that the shorter wavelength disperses over a smaller, thinner area on the target, which leads to the ablation of a smaller amount of materials; as a result, smaller nanoparticles are generated in the solution. In contrast, the longer wavelength disperses more widely in the target material, leading to the ablation of more materials, which in turn generates larger nanoparticles. Furthermore, the inter-particle separation can be seen clearly among the Au nanoparticles produced at 532 nm, whereas almost all of the Au nanoparticles produced at 1064 nm are stuck together, forming chains. Rong et al. [40, 41] showed that if the inter-particle separations (Δ) are larger than the particle diameter (D) ($\Delta > D$), “the near-field interaction between the particles is small and the resonance wavelength λ_{res} is that of an individual particle”, but if the inter-particle

separations are smaller than the particle diameter ($\Delta < D$), “the plasmons in the individual particles couple and the resonance wavelength λ_{res} red shifts with decreasing separation”. They observed the red-shift phenomena while increasing the intensity ratio ($R = I_{580 \text{ nm}}/I_{530 \text{ nm}}$). Here red-shift phenomena of the Au nanoparticles’ optical absorption spectra can be seen with the longer laser wavelength because the nanoparticles produced at the longer wavelength are joined together and there is no distance between them. Giorgetti et al. [10] attributed the different wavelengths to the production of different sizes of Au nanoparticles by picosecond laser ablation in water, as well as the different ablation mechanisms, and suggested that “at higher energy per pulse, and correspondingly higher fluence, material extraction by multiphoton absorption dominates over heating effects”.

Haustrup and O’Connor [42] identified the existence of a linear relationship between the size of the Au nanoparticles and the size of the grain produced at both 343 and 515 nm wavelengths, whereas there is no relationship at 1030 nm wavelength ablation. This is due to the inter-band absorption effects at the shorter wavelengths, which results in faster electron–phonon coupling and higher electron temperatures that process produces thermoelastic stresses in the target material. On the other hand, no inter-band absorption occurs at a wavelength of 1030 nm; thus, the absorption occurs by intra-band absorption and the ablation process takes place over longer timescales, resulting in the removal of the grain boundaries prior to production of the nanoparticles [42].

A problem with comparing the effect of different wavelengths in producing nanoparticles in a liquid solution is the different beam absorption characteristics of the nanoparticles at different laser wavelengths. For example, Ag nanoparticles are more efficient for self-absorption at the 532-nm wavelength than at the 1064-nm wavelength because of the surface plasmon bands that form at around 400 nm [3]. In addition, the absorption coefficient α is a function of the wavelength.

Different laser wavelengths also have different responses to energy loss within the water above the target materials. As a result different size of the nanoparticles would be produced, if the energy loss was not corrected. As shown in Fig. 11, it can be seen that the water level has a strong effect on the laser power at the 1064-nm wavelength, while it has a negligible effect at the 532-nm wavelength. For example, at a 2-mm water level, about 5.5 and 0.004 % of the laser power will be lost at 1064 and 532 nm wavelengths, respectively. This is because water has a strong absorption coefficient at 1064 nm and a weak absorption coefficient at 532 nm. The relationship between laser power loss (expressed as a percentage) and water level is linear for both wavelengths.

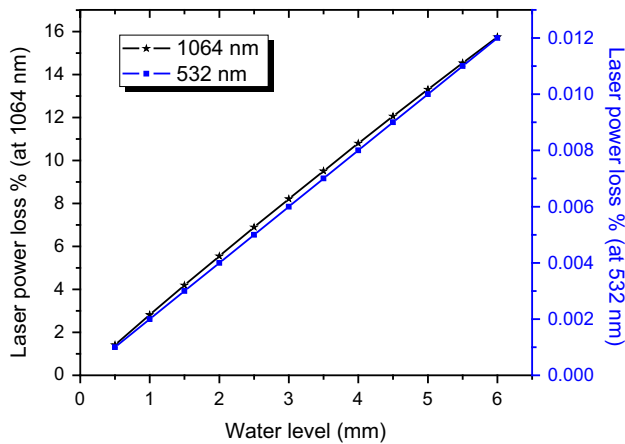


Fig. 11 Laser power loss at 532 and 1064 nm wavelengths due to water level above the sample during generation of nanoparticles

The laser beam focal length will be increased in water. As shown in Fig. 12a, the amount of increased focal length is directly proportional to the water height. In water, the focal length will be increased when it passes through a liquid medium. This effect is increased during ablation under water at ultra-short wavelengths such as picosecond and femtosecond lasers due to refraction and self-focusing inside the liquid medium [43, 44].

The focal length will increase according to the following equation [44]:

$$\Delta f = l \left(1 - \frac{1}{n} \right) \tag{1}$$

In the above equation Δf is the amount by which the focal length increases in water, l is the water level above the target material, and n is the refractive index of the liquid medium. This fraction of focal length must be compensated while focusing the laser beam on the target

material in the water; in other words, the distance between the lens and the target should be increased depending on the height of the liquid above the sample. As shown in Fig. 12a, the amount of increased focal length is directly proportional to the water height. This effect is the same at both 532 and 1064 nm because focal length does not depend on the wavelength.

While focusing the laser beam on the target sample in water, the distance between the scan head and the target material should be increased (see Fig. 12b). For example, at a water level of 2 mm above the sample, the focal distance should be increased by about 0.5 mm and for 4 mm this distance should be 1 mm. It is worth mentioning that the focal length of the laser-focusing lens and the position of the target material have a significant effect on the size distribution and the shape of the nanoparticles produced [2].

Refractive index declines with the increase in wavelength, so a smaller refractive index means higher laser beam refraction in the media leads to change the ablation area (or marking area) in comparison with the program made marking area. This could explain why a smaller scanned area was produced on the target surface in comparison with the CNC program made. Here, at 532 nm, the laser produced smaller scan area than the 1064-nm wavelength. Here, 1064 nm produced larger scan area than the 532-nm wavelength because the longer wavelength gives smaller change in refractive index. Due to this reason longer laser wavelength leads to considerably higher ablation efficiency [45].

4.2 Effects of Wavelengths on the Crystallinity of Metal Oxide Nanoparticles

XRD patterns show that the iron oxide nanoparticles are crystalline with mixed Fe, FeO and Fe₃O₄. FeO may be

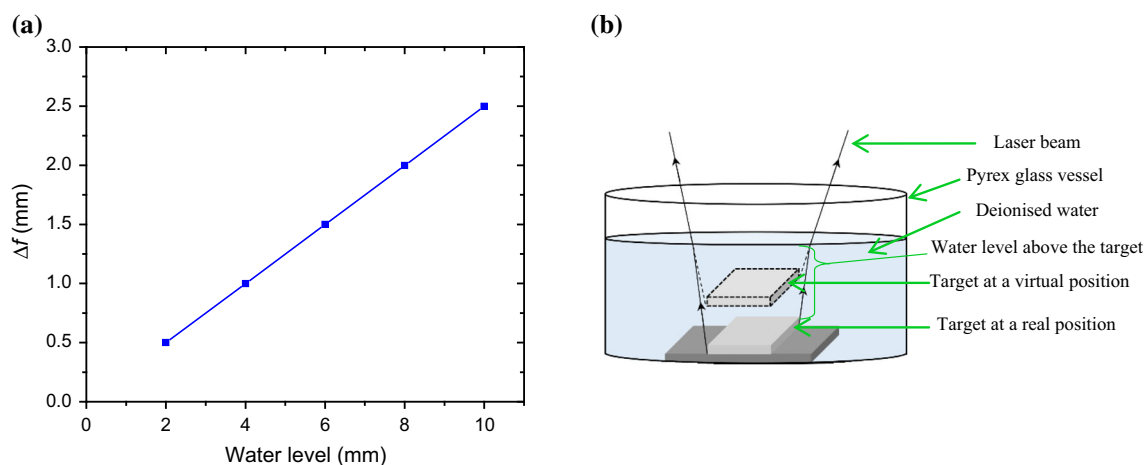


Fig. 12 Increase in focal length of the lens of a laser tool as a function of height above water level (a). Real and virtual depth of the target material (b)

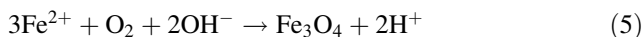
produced according to Eqs. (2) and (3) [16]. The interaction between the laser beam and the Fe target material produces Fe clusters. Then they will interact with the liquid solution leading to the production of Fe(OH)₂ and hydrogen release. Due to the high temperature and high pressure at the target–liquid interface, FeO would be produced [16].



Because Fe exists in a wide range of oxidation states, redox reactions must be taken into account. The existence of the different types iron oxides dependent upon to different redox reactions [46].



As shown in Eq. (5), Fe₃O₄ can be produced by controlled oxidation of Fe²⁺ in solution:



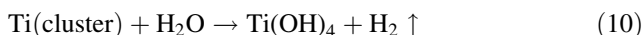
Zero-valent iron (Fe⁰) can be obtained according to Eq. (6) [47]:



During laser interaction with the Zn target material in deionised water, ZnO nanoparticles could be produced according to the following equations [48].



After laser interaction with the Ti target, Ti cluster or Ti vapour will be produced; then, they interacted with water to produce titanium (IV) hydroxide Ti(OH)₄. Finally, TiO₂ nanoparticles will be produced according to Eqs. (10) and (11) [49].



XRD characterisation shows that the crystallinity of titanium dioxide is strongly dependent upon the laser wavelengths, as the formation of the titanium dioxide phases (anatase, rutile and brookite) depends on temperature. Iron oxide nanoparticles are slightly dependent upon the laser wavelength, but the wavelength has no effect on crystalline ZnO nanoparticles. In other words, the oxide materials with more crystalline phases are affected by laser wavelength. XRD patterns show that the TiO₂ nanoparticles produced at a wavelength of 532 nm are more crystalline than those produced at 1064 nm. The wavelength of 532 nm can produce mixed anatase, rutile and brookite phases of TiO₂ nanoparticles, but the wavelength of 1064 nm can only produce rutile and brookite phases. A

strong rutile peak was observed at optical absorption spectra of 532 nm at 27.5°. In addition, some small peaks of the anatase and rutile phases were observed at the 532-nm wavelength. These small peaks were produced when the sample was annealed at 500 and 800 °C for 2 h. According to the last case, the 532-nm laser wavelength may produce a higher temperature than the 1064 nm. Crystalline phases are easily produced within materials that have a low phase-transition temperature [50].

Phase transition of the TiO₂ is not only affected by wavelength, but also by the laser beam mode such as pulsed or continuous wave (CW). Single-phase rutile TiO₂ was obtained at 553–952 °C using a CW CO₂ laser at 1064 nm wavelength, while the rutile changed to anatase with increasing deposition temperature from 579 to 957 °C using a Nd:YAG laser at 1064 nm [51].

The laser power and the type of target material are important in order to control the uniformity of the iron oxide phases. Furthermore, liquid environments have an effect on the crystallinity of the iron oxide phases; for example, in this work, crystalline maghemite (α-Fe₂O₃) nanoparticles were not produced because of the use of deionised water. Conversely, laser ablation of an iron oxide target material in acetone and ethanol produces crystalline maghemite (γ-Fe₂O₃) nanoparticles [52]. The crystallinity of the iron oxide nanoparticles increases with increasing laser energy [53]. However, for better understanding, further study of this topic is required.

5 Conclusions

This study has investigated the effects of two laser wavelengths (532 and 1064 nm) of a picosecond laser on the size and size distribution of the Au, Ag, Ag–TiO₂, TiO₂, ZnO and iron oxide nanoparticles in deionised water. The results show that slightly smaller metal oxide nanoparticles (TiO₂, ZnO and iron oxide) were produced at the 1064-nm wavelength. In spite of higher laser fluence at 532 nm than that at 1064 nm, significant reduction of particle size was seen for the production of pure Au and Ag–TiO₂ nanoparticles at the 532-nm wavelength showing more dominating effect of laser wavelength. Pure Ag nanoparticles could not be produced at the 532-nm laser wavelength of the picosecond laser, but Ag–TiO₂ nanoparticles were produced by using a Ti/Ag alloy as a target material. It was found that the water level above the target material does not have a significant effect on the loss of laser intensity at the 532-nm wavelength, but at 1064 nm wavelength the laser intensity was significantly reduced. It was also found that the formation of crystalline TiO₂ nanoparticles was strongly dependent upon the wavelength.

Open Access This article is distributed under the terms of the Creative Commons Attribution 4.0 International License (<http://creativecommons.org/licenses/by/4.0/>), which permits unrestricted use, distribution, and reproduction in any medium, provided you give appropriate credit to the original author(s) and the source, provide a link to the Creative Commons license, and indicate if changes were made.

References

1. R. Singh, R. Soni, Improved catalytic activity of laser generated bimetallic and trimetallic nanoparticles. *J. Nanosci. Nanotechnol.* **14**(9), 6872–6879 (2014)
2. H. Imam, K. Elsayed, M.A. Ahmed, R. Ramdan, Effect of experimental parameters on the fabrication of gold nanoparticles via laser ablation. *Opt. Photonics J.* **2**, 73–82 (2012)
3. F. Hajiesmaeilbaigi, A. Mohammadalipour, J. Sabbaghzadeh, S. Hoseinkhani, H. Fallah, Preparation of silver nanoparticles by laser ablation and fragmentation in pure water. *Laser Phys. Lett.* **3**(5), 252 (2006)
4. A. Baladi, R.S. Mamoory, Study on wavelength and energy effects on pulsed laser ablation synthesis of aluminum nanoparticles in ethanol, in *MEMS, NANO, and Smart Systems (ICMENS), 2009 Fifth International Conference on 2009*: IEEE (2009)
5. S.Z. Mortazavi, P. Parvin, A. Reyhani, A.N. Golikand, S. Mirershadi, Effect of laser wavelength at IR (1064 nm) and UV (193 nm) on the structural formation of palladium nanoparticles in deionized water. *J. Phys. Chem. C* **115**(12), 5049–5057 (2011)
6. J. Kim, D.A. Reddy, R. Ma, T.K. Kim, The influence of laser wavelength and fluence on palladium nanoparticles produced by pulsed laser ablation in deionized water. *Solid State Sci.* **37**, 96–102 (2014)
7. P. Chewchinda, T. Tsuge, H. Funakubo, O. Odawara, H. Wada, Laser wavelength effect on size and morphology of silicon nanoparticles prepared by laser ablation in liquid. *Jpn. J. Appl. Phys.* **52**(2R), 025001 (2013)
8. C. He, T. Sasaki, Y. Shimizu, N. Koshizaki, Synthesis of ZnO nanoparticles using nanosecond pulsed laser ablation in aqueous media and their self-assembly towards spindle-like ZnO aggregates. *Appl. Surf. Sci.* **254**(7), 2196–2202 (2008)
9. R. Intartaglia, G. Das, K. Bagga, A. Gopalakrishnan, A. Genovese, M. Povia, E. Di Fabrizio, R. Cingolani, A. Diaspro, F. Brandi, Laser synthesis of ligand-free bimetallic nanoparticles for plasmonic applications. *Phys. Chem. Chem. Phys.* **15**(9), 3075–3082 (2013)
10. E. Giorgetti, A. Giusti, F. Giammanco, P. Marsili, S. Laza, Dendrimer-capped nanoparticles prepared by picosecond laser ablation in liquid environment. *Molecules* **14**(9), 3731–3753 (2009)
11. A. Hamad, L. Li, Z. Liu, X.L. Zhong, H. Liu, T. Wang, Generation of silver titania nanoparticles from an Ag–Ti alloy via picosecond laser ablation and their antibacterial activities. *RSC Adv.* **5**(89), 72981–72994 (2015)
12. A. Hamad, L. Li, Z. Liu, A comparison of the characteristics of nanosecond, picosecond and femtosecond lasers generated Ag, TiO₂ and Au nanoparticles in deionised water. *Appl. Phys. A* **120**(4), 1247–1260 (2015)
13. A. Schwenke, P. Wagener, S. Nolte, S. Barcikowski, Influence of processing time on nanoparticle generation during picosecond-pulsed fundamental and second harmonic laser ablation of metals in tetrahydrofuran. *Appl. Phys. A* **104**(1), 77–82 (2011)
14. K. Nouneh, M. Oyama, G. Lakshminarayana, I. Kityk, A. Wojciechowski, K. Ozga, Kinetics of picosecond laser treatment of silver nanoparticles on ITO substrate. *J. Alloys Compd.* **509**(40), 9663–9668 (2011)
15. A. Menéndez-Manjón, A. Schwenke, T. Steinke, M. Meyer, U. Giese, P. Wagener, S. Barcikowski, Ligand-free gold–silver nanoparticle alloy polymer composites generated by picosecond laser ablation in liquid monomer. *Appl. Phys. A* **110**(2), 343–350 (2013)
16. P. Liu, W. Cai, H. Zeng, Fabrication and size-dependent optical properties of FeO nanoparticles induced by laser ablation in a liquid medium. *J. Phys. Chem. C* **112**(9), 3261–3266 (2008)
17. T.K. Ghorai, Synthesis of spherical mesoporous titania modified iron-niobate nanoclusters for photocatalytic reduction of 4-nitrophenol. *J. Mater. Res. Technol.* **4**(2), 133–143 (2015)
18. P. Anandgaonker, G. Kulkarni, S. Gaikwad, A. Rajbhoj, Nanocrystalline titanium dioxide catalyst for the synthesis of azlactones. *Chin. J. Catal.* **35**(2), 196–200 (2014)
19. J. Yan, G. Wu, N. Guan, L. Li, Z. Li, X. Cao, Understanding the effect of surface/bulk defects on the photocatalytic activity of TiO₂: anatase versus rutile. *Phys. Chem. Chem. Phys.* **15**(26), 10978–10988 (2013)
20. T.A. Kandiel, L. Robben, A. Alkaim, D. Bahnemann, Brookite versus anatase TiO₂ photocatalysts: phase transformations and photocatalytic activities. *Photochem. Photobiol. Sci.* **12**(4), 602–609 (2013)
21. Y. Li, N.-H. Lee, D.-S. Hwang, J.S. Song, E.G. Lee, S.-J. Kim, Synthesis and characterization of nano titania powder with high photoactivity for gas-phase photo-oxidation of benzene from TiOCl₂ aqueous solution at low temperatures. *Langmuir* **20**(25), 10838–10844 (2004)
22. K. Gupta, R. Singh, A. Pandey, A. Pandey, Photocatalytic antibacterial performance of TiO₂ and Ag-doped TiO₂ against *S. aureus*, *P. aeruginosa* and *E. coli*. *Beilstein. J. Nanotechnol.* **4**(1), 345–351 (2013)
23. Y. Li, J. Li, M. Ma, Y. Ouyang, W. Yan, Preparation of TiO₂/activated carbon with Fe ions doping photocatalyst and its application to photocatalytic degradation of reactive brilliant red K2G. *Sci. China, Ser. B: Chem.* **52**(8), 1113–1119 (2009)
24. S.S. Mukunda-Rao, K. Natarajan, Antibiofilm Activity of Epoxy/Ag-TiO₂ Polymer Nanocomposite Coatings against *Staphylococcus aureus* and *Escherichia coli*, in *Photocatalytic Coatings for Air-Purifying, Self-Cleaning and Antimicrobial Properties*, ed. by A. Maury-Ramirez (MDPI, Basel, Switzerland, 2015), p. 3
25. P. Ramasamy, D.-M. Seo, S.-H. Kim, J. Kim, Effects of TiO₂ shells on optical and thermal properties of silver nanowires. *J. Mater. Chem.* **22**(23), 11651–11657 (2012)
26. Lopez, J.A., F. González, F.A. Bonilla, G. Zambrano and M.E. Gómez, Synthesis and characterization of Fe₃O₄ magnetic nanofluid. *Rev. Latinoam. Metal. Mater.* **30**(1), 60–66 (2010)
27. S. Wu, A. Sun, F. Zhai, J. Wang, W. Xu, Q. Zhang, A.A. Volinsky, Fe₃O₄ magnetic nanoparticles synthesis from tailings by ultrasonic chemical co-precipitation. *Mater. Lett.* **65**(12), 1882–1884 (2011)
28. S. Sharma, J. Vargas, K. Pirotta, S. Kumar, C. Lee, M. Knobel, Synthesis and ageing effect in FeO nanoparticles: transformation to core–shell FeO/Fe₃O₄ and their magnetic characterization. *J. Alloys Compd.* **509**(22), 6414–6417 (2011)
29. Y. Hou, Z. Xu, S. Sun, Controlled synthesis and chemical conversions of FeO nanoparticles. *Angew. Chem.* **119**(33), 6445–6448 (2007)
30. R.J. Joseyphus, K. Shinoda, D. Kodama, B. Jeyadevan, Size controlled Fe nanoparticles through polyol process and their magnetic properties. *Mater. Chem. Phys.* **123**(2), 487–493 (2010)
31. Z. Yuanbi, Q. Zumin, J. Huang, Preparation and analysis of Fe₃O₄ magnetic nanoparticles used as targeted-drug carriers. *Chin. J. Chem. Eng.* **16**(3), 451–455 (2008)

32. R. Gabbasov, M. Polikarpov, V. Cherepanov, M. Chuev, I. Mischenko, A. Lomov, A. Wang, V. Panchenko, Mössbauer, magnetization and X-ray diffraction characterization methods for iron oxide nanoparticles. *J. Magn. Magn. Mater.* **380**, 111–116 (2015)
33. R.M. Alwan, Q.A. Kadhim, K.M. Sahan, R.A. Ali, R.J. Mahdi, N.A. Kassim, A.N. Jassim, Synthesis of zinc oxide nanoparticles via sol–gel route and their characterization. *Nanosci. Nanotechnol.* **5**(1), 1–6 (2015)
34. Y.T. Prabhu, K.V. Rao, V.S.S. Kumar, B.S. Kumari, Synthesis of ZnO Nanoparticles by a novel surfactant assisted amine combustion method. *Adv. Nanoparticles* **2**(01), 45 (2013)
35. M.R. Arefi, S. Rezaei-Zarchi, Synthesis of zinc oxide nanoparticles and their effect on the compressive strength and setting time of self-compacted concrete paste as cementitious composites. *Int. J. Mol. Sci.* **13**(4), 4340–4350 (2012)
36. S. Dutta, B.N. Ganguly, Characterization of ZnO nanoparticles grown in presence of Folic acid template. *J. Nanobiotechnol.* **10**(1), 1–10 (2012)
37. A. Hamad, L. Li, Z. Liu, X.L. Zhong, G. Burke, T. Wang, The characteristics of novel bimodal Ag–TiO₂ nanoparticles generated by hybrid laser-ultrasonic technique. *Appl. Phys. A* **122**(4), 1–12 (2016)
38. M. Takahashi, Y. Takada, M. Kikuchi, O. Okuno, Released ions and microstructures of dental cast experimental Ti–Ag alloys, in *Interface Oral Health Science 2007* (Springer, 2007), pp. 311–316
39. U. Gurudas, E. Brooks, D.M. Bubb, S. Heiroth, T. Lippert, A. Wokaun, Saturable and reverse saturable absorption in silver nanodots at 532 nm using picosecond laser pulses. *J. Appl. Phys.* **104**(7), 73107 (2008)
40. G. Rong, H. Wang, L.R. Skewis, B.M. Reinhard, Resolving sub-diffraction limit encounters in nanoparticle tracking using live cell plasmon coupling microscopy. *Nano Lett.* **8**(10), 3386–3393 (2008)
41. G. Rong, H. Wang, B.M. Reinhard, Insights from a nanoparticle minuet: two-dimensional membrane profiling through silver plasmon ruler tracking. *Nano Lett.* **10**(1), 230–238 (2009)
42. N. Hastrup, G. O'Connor, Impact of wavelength dependent thermo-elastic laser ablation mechanism on the generation of nanoparticles from thin gold films. *Appl. Phys. Lett.* **101**(26), 263107 (2012)
43. A. Menéndez-Manjón, P. Wagener, S. Barcikowski, Transfer-matrix method for efficient ablation by pulsed laser ablation and nanoparticle generation in liquids. *J. Phys. Chem. C* **115**(12), 5108–5114 (2011)
44. Z. Yan, D.B. Chrisey, Pulsed laser ablation in liquid for micro-/nanostucture generation. *J. Photochem. Photobiol. C Photochem. Rev.* **13**(3), 204–223 (2012)
45. A. Baladi, R.S. Mamoory, Effect of laser wavelength and ablation time on pulsed laser ablation synthesis of Al nanoparticles in ethanol, in *International Journal of Modern Physics: Conference Series*. 2012: World Scientific
46. R. Bosinceanu, N. Sulitanu, Synthesis and characterization of FeO(OH)/Fe₃O₄ nanoparticles encapsulated in zeolite matrix. *J. Optoelectron. Adv. Mater.* **10**(12), 3482–3486 (2008)
47. Y.-P. Sun, X.-Q. Li, J. Cao, W.-X. Zhang, H.P. Wang, Characterization of zero-valent iron nanoparticles. *Adv. Colloid Interface Sci.* **120**(1), 47–56 (2006)
48. M. Gondal, Q. Drmosh, Z. Yamani, T. Saleh, Synthesis of ZnO₂ nanoparticles by laser ablation in liquid and their annealing transformation into ZnO nanoparticles. *Appl. Surf. Sci.* **256**(1), 298–304 (2009)
49. S.M. Hong, S. Lee, H.J. Jung, Y. Yu, J.H. Shin, K.-Y. Kwon, M.Y. Choi, Simple Preparation of Anatase TiO₂ Nanoparticles via pulsed laser ablation in liquid. *Bull. Korean Chem. Soc.* **34**, 279–282 (2013)
50. A.V. Kolobov, *Photo-induced metastability in amorphous semiconductors* (Wiley, Chichester, 2006)
51. M. Gao, A. Ito, T. Goto, Effect of laser wavelength on phase and microstructure of TiO₂ films prepared by laser chemical vapor deposition. *Surf. Coat. Technol.* **244**, 166–172 (2014)
52. P. Maneeratanasarn, T.V. Khai, S.Y. Kim, B.G. Choi, K.B. Shim, Synthesis of phase-controlled iron oxide nanoparticles by pulsed laser ablation in different liquid media. *Phys. Status Solidi (a)* **210**(3), 563–569 (2013)
53. P. Maneeratanasarn, T. Khai, B. Choi, K. Shim, The effect of laser energy on the preparation of iron oxide by a pulsed laser ablation in ethanol. *J. Korean Cryst. Growth Cryst. Technol.* **22**(3), 134–138 (2012)